Supplemental information

October 21, 2024

1 Supplemental Note 1: Labeling data of battery aging modes

It has been experimentally validated that the three aging modes, i.e., LLI, $\mathrm{LAM_{PE}}$, and $\mathrm{LAM_{NE}}$, can be identified and quantified from pseudo-OCV measurements of a battery cell [1]. For the training of Model 2, we employ the diagnostic algorithm from [1] to label all aging mode data over the battery's lifespan, using the cell's pseudo-OCV obtained during the RPT test (specified in Section 5.1.3 of the main text) and the OCV-related parameters and functions in the SPMe battery model. The details are introduced in the remainder of this section.

The cell OCV, $U_{\mathrm{ocv}}(\mathrm{SoC})$, is defined as the difference between the positive electrode OCP curve (U_P) and the negative electrode OCP curve (U_N), i.e.,

$$U_{\mathrm{OCV}}(\mathrm{SoC}) = U_P(\theta^+) - U_N(\theta^-), \tag{1}$$

where θ^+ and θ^- are stoichiometric variables, indicating the lithiation level of the positive and negative electrodes, respectively. Usually, the cell is operated between the predefined cut-off voltage levels U_h and U_l, which are defined as

$$U_h = U_P(\theta^+_{\mathrm{EOC}}) - U_N(\theta^-_{\mathrm{EOC}}), \tag{2}$$

$$U_l = U_P(\theta^+_{\mathrm{EOD}}) - U_N(\theta^-_{\mathrm{EOD}}). \tag{3}$$

By consolidating (1)–(3), the cell OCV at time t can be represented as a static function of $\mathrm{SoC}(t)$, θ^+_{EOC}, and θ^-_{EOD}, as given by

$$U_{\mathrm{OCV}}(t) = f_{\mathrm{OCV}}\left(\mathrm{SoC}(t), \theta^+_{\mathrm{EOC}}, \theta^-_{\mathrm{EOD}}\right), \tag{4}$$

where θ^+_{EOC} and θ^-_{EOD} are aging-related parameters and considered constants within the period of a charge. The analytical form of $f_{\mathrm{OCV}}()$ can be derived from (1)–(3).

Once U_{OCV} is measured and SoC is estimated, e.g., using the method developed in [2], then θ^+_{EOC} and θ^-_{EOD} can be identified by solving the following optimization problem that minimizes the difference between the measured OCV, $\bar{U}_{\mathrm{OCV}}$, and the estimated OCV

$$[\theta^{+,*}_{\mathrm{EOC}}, \theta^{-,*}_{EOD}] = \arg\min_{\theta^+_{\mathrm{EOC}}, \theta^-_{\mathrm{EOD}}} \int_{t_0}^{t_{end}} \left[\bar{U}_{\mathrm{OCV}}(t) - f_{\mathrm{OCV}}\left(\mathrm{SoC}(t), \theta^+_{\mathrm{EOC}}, \theta^-_{\mathrm{EOD}}\right)\right]^2 dt, \tag{5}$$

where t_0 and t_{end} are the starting and end time for slow charging events, respectively. Solving such an optimization problem periodically as the battery is gradually aging, the stoichiometric parameters of the positive and negative electrodes can be acquired and used to quantify the battery degradation modes through the following two-step scheme:

Firstly, the lithium inventory (LI) of the battery at the current cycle number l can be calculated as the sum of the usable lithium inventory in the positive and negative electrodes, i.e.,

$$\mathrm{LI}_l = \mathrm{LI}^+_l + \mathrm{LI}^-_l, \tag{6}$$

$$\mathrm{LI}^+_l = \frac{C_l}{\theta^+_{\mathrm{EOD},l} - \theta^+_{\mathrm{EOC},l}}\theta^+, \tag{7}$$

$$\mathrm{LI}^-_l = \frac{C_l}{\theta^-_{\mathrm{EOC},l} - \theta^-_{\mathrm{EOD},l}}\theta^-, \tag{8}$$

where LI_l^+ and LI_l^- are the lithium inventory in the positive and negative electrode, respectively, and C_l is the battery cell capacity. Then, the LLI can be calculated as

$$\mathrm{LLI} = 1 - \frac{\mathrm{LI}_l}{\mathrm{LI}_0}, \tag{9}$$

where LI_0 is the lithium inventory when the battery is new.

Secondly, the LAM will theoretically lead to a shrinking of the OCP [1] and, correspondingly, a reduction of the usable capacity in the electrode that can be represented as

$$\mathrm{LAM}_{\mathrm{PE}} = 1 - \frac{C_l^+}{C_0^+}, \tag{10}$$

$$C_l^+ = \frac{C_l}{\theta^+_{\mathrm{EOD},\,l} - \theta^+_{\mathrm{EOC},l}}, \tag{11}$$

$$\mathrm{LAM}_{\mathrm{NE}} = 1 - \frac{C_l^-}{C_0^-}, \tag{12}$$

$$C_l^- = \frac{C_l}{\theta^-_{\mathrm{EOC},l} - \theta^-_{\mathrm{EOD},l}}, \tag{13}$$

where C_0^+ and C_0^- represent the initial capacity of the positive and negative electrodes, respectively.

Noteworthy, the scheme above for quantifying battery degradation modes requires solving the nonlinear optimization problem formulated in (1)–(5) in real-time. This process is not only computationally expensive but also requires the battery to operate in its full SoC window jointly defined by θ^+_{EOC}, θ^-_{EOC}, θ^+_{EOD}, and θ^-_{EOD}, which is not practically viable for real-world vehicle applications. Consequently, we only use this scheme to label data samples in the training set and propose an ML-based method, i.e., Model 2, to estimate these aging modes for real-world usage.

2 Supplemental Note 2: Implementation and comparative analysis for SoH indicator estimation

2.1 Implementation of Model 1

Features. The methodology employed for estimating battery capacity in this study aligns closely with the machine learning (ML) framework delineated in [3]. The comprehensive feature pool used in this work is presented below. First, the total charging time between the designated SoC window is selected, as it will gradually change as the battery degrades. Secondly, the energy value of the current and voltage are also selected and are calculated using the following equation

$$E = \int_0^\infty s(t)^2 \, dt, \tag{14}$$

where $s(t)$ is the signal, manifesting as the current and voltage in this context. Thirdly, the integrals of the current and voltage curves are deemed to be reflective of the battery's aging process and, hence, are selected for inclusion in the feature set. Fourthly, the evolving steepness of the voltage curve, which becomes more pronounced with aging, is also considered a vital feature. Finally, the temperature is acknowledged as a significant factor influencing overall battery behavior and is therefore incorporated into the feature array. For the histogram-usage-related features, accumulated energy throughput is calculated between each RPT cycle to form the input for the one-step-ahead prediction model.

ML algorithms. In total, four distinct ML algorithms are included in the pipeline. Two of them are probabilistic-based, namely Gaussian process regression (GPR) and Bayesian regression (BR), and the other two are frequentist-based, which are random forest regression (RFR) and artificial neural network (ANN).

2.2 Benchmarks for SoH indicators

The first type of benchmark is to a single LSTM model whose outputs are the four SoH indicators, and the inputs are the same as those of Model 2. The hyperparameters used for the LSTM are listed in Table S1. The second

type of benchmark includes linear regression (LR), Elastic net (EN), GPR, BR, RFR, and ANN. For each of these point-to-point estimation models, the features constructed from time-series data in Section 2.1 are used as inputs, and the four SoH indicators are outputs.

Table S1: Hyperparameters of the LSTM in Model 2.

Parameter name	Parameter value range
First LSTM layer cell number	16
Output LSTM layer cell number	1
Learning rate	0.001
Batch size	256
Early stopping	25
Epochs	100

2.3 Comparative analysis

Capacity estimation. The results of battery capacity estimation utilizing Model 1 and its two types of benchmarks are presented in Table S2. The Kalman filter (KF)-based model fusion algorithm performs equally well as the best-performed ML algorithm, i.e., GPR, and surpasses all the other individual ML algorithms in battery capacity estimation. This demonstrates the improved estimation accuracy and robustness of our developed Model 1.

Table S2: Comparison of the proposed algorithm with two benchmarks for battery state of health (SoH) capacity estimation.

Metrics	The proposed	Benchmarks of type 1						Benchmarks of type 2
	Model fusion	LR	EN	GPR	BR	RFR	ANN	LSTM
MAE (%)	**0.077**	0.228	0.273	0.077	0.346	0.298	3.751	0.918
RMSE (%)	**0.131**	0.295	0.374	0.131	0.445	0.451	4.616	0.978

Aging mode quantification. The comparative results of Model 2 against its benchmarks (i.e., the type 1 benchmarks introduced in Section 2.2) for quantifying the three aging modes are presented in Table S3. The data reveals that the LSTM model exhibits superior accuracy in estimating $\mathrm{LAM_{NE}}$ and $\mathrm{LAM_{PE}}$. In the case of LLI, the LSTM model's performance is marginally outpaced by the best-performing RFR model, with a difference of 0.091% in MAE. Based on such results, we, therefore, select LSTM in Model 2 for battery aging mode quantification.

Table S3: Comparison of different ML algorithms on battery aging modes estimation results

Evaluation metrics	Degradation mode	LR	EN	GPR	BR	RFR	ANN	LSTM
MAE (%)	$\mathrm{LAM_{NE}}$	1.888	3.308	0.958	1.888	0.876	2.912	**0.375**
	$\mathrm{LAM_{PE}}$	0.693	2.245	0.289	0.693	0.366	1.371	**0.269**
	LLI	0.349	1.069	0.139	0.348	**0.109**	0.581	0.200
RMSE (%)	$\mathrm{LAM_{NE}}$	2.973	5.151	1.436	2.973	2.201	4.886	**0.546**
	$\mathrm{LAM_{PE}}$	1.038	3.892	0.513	1.038	0.804	2.312	**0.439**
	LLI	0.349	1.069	0.245	0.520	**0.238**	0.971	0.289

3 Supplemental Note 3: Model 3 versus benchmarks for plating potential estimation

In addition to Model 3, which incorporates our proposed underestimate-enhanced long short-term memory (UE-LSTM) network, this study also implements three other ML-based models for comparative analysis, i.e., a gated recurrent unit (GRU) neural network, an ANN and a transformer. The hyperparameters used for each algorithm are detailed in Table S4.

Table S4: Hyperparameters of the models for plating potential estimation

Model	Parameter name	Parameter value range
UE-LSTM	First LSTM layer cell number	16
	Output LSTM layer cell number	1
	Learning rate	0.005
	Batch size	256
	Early stopping	25
	Epochs	200
GRU	First GRU layer cell number	16
	Output GRU layer cell number	1
	Learning rate	0.005
	Batch size	256
	Early stopping	25
	Epochs	200
ANN	First dense layer neuron number	4096
	Second dense layer neuron number	1024
	Third dense layer neuron number	128
	Fourth dense layer neuron number	32
	Learning rate	0.005
	Batch size	100000
	Early stopping	25
	Epochs	200
Transformer	Number of heads	4
	Model dimension	32
	Feedforward dimension	64
	Number of layers	2
	Dropout rate	0.01
	Learning rate	0.002
	Batch size	256
	Early stopping	25
	Epochs	200

Table S5 delineates the comparative results of these three ML models for plating potential estimation over the same test set. Our proposed UE-LSTM model stands out by achieving the lowest errors and the highest computational efficiency. The GRU model, while slightly inferior to UE-LSTM, still maintains a commendable level of accuracy and efficiency. This distinction in performance is attributable to the fact that both UE-LSTM and GRU, as recurrent neural networks, process the entire time series data in a unified manner, thus efficiently managing long-term dependencies, retaining state information across sequences, and offering enhanced comprehension of the temporal context in the data. Conversely, the ANN model, constrained by its inability to process the entire time series data simultaneously, resorts to analyzing individual time points independently for estimations. This approach not only diminishes the accuracy of the results but also necessitates extended durations for training and testing. The Transformer model, while slightly closer in accuracy than GRU, still trails the LSTM with an MAE of 4.01 mV and an RMSE of 5.91 mV. This suggests that although the Transformer performs better than ANN, it does not surpass LSTM or GRU in this estimation task. Regarding the Transformer model, we recognize that with more extensive tuning, there is a possibility that its performance could match or even surpass that of the LSTM. However, given the complexity and large number of hyperparameters in the Transformer architecture, we adopted a random search approach for hyperparameter tuning, testing 100 different configurations. The values reported represent the best results from this search. Despite this effort, the Transformer did not achieve the same level of accuracy as the LSTM, and it also required more computational resources. This highlights the balance between model complexity and practical performance in this context, reinforcing the value of using LSTM for estimating battery plating potential.

Table S5: Comparison of LSTM and its three benchmarks in the estimation of battery plating potential.

Evaluation metrics	GRU	ANN	Transformer	UE-LSTM
MAE (mV)	3.40	10.43	4.01	**3.37**
RMSE(mV)	4.82	16.36	5.91	**4.77**
Training time (s)	856	1128	1898	**680**
Testing time (s)	3.13	69.71	83	**2.87**

4 Supplemental Note 4: Electrode materials information

The electrode materials used in the three-electrode experiments are bought from CUSTOMCELLS Holding GmbH. The cathode is composed of lithium nickel manganese cobalt (NMC) oxide, and the anode is composed of artificial graphite. The detailed information is summarized in Table S6.

Table S6: Specifications for battery active materials.

	Cathode	Anode
Material	NMC811	Artificial Graphite
Active material content (%)	96	95
Specific capacity (mAh/g)	175	355
Collector foil type	Aluminum	Copper
Collector foil thickness (μm)	20	14
Nominal Voltage (V)	3.7	0.1
Area capacity (mAh/cm^2)	2	2.5
Density (g/cm^3)	2.9	1.7
Porosity (%)	38	25

5 Supplemental Note 5: Parameters of the employed SPMe-aging battery model

The parameter values for the physics-based are taken from [4], and the battery specification is presented in Table S7. Table S8 lists temperature and aging-related parameters that are altered to generate different aging trajectories. The visualization of the simulation results are shown in Fig. S1. It can be seen that many cells demonstrate distinct patterns of capacity degradation, with clear non-linear characteristics. Similarly, the SoH indicators exhibit pronounced non-linearity over the cycle life, as visualized in Supplemental Information Fig. S2.

Table S7: Technical specifications of LG M50T battery cell.

Cathode	NMC811
Anode	Graphite with 10% SiO_x
Nominal capacity	5 Ah
Voltage range	2.5–4.2 V
Operating temperature	-20–50 °C

6 Supplemental Note 6: Additional estimation results from Models 1 and 2

Figs. S3–S8 present additional estimation results for the four targeted SoH indicators using Models 1 and 2, in which different partial SoC operating windows have been used.

Table S8: EM parameter values used for synthetic data generation.

Parameter name	Parameter value range
SEI exchange current density $i_{0,sei}$	[0, 1e-15, 1e-14, 1e-13, 1e-12]
LAM_{PE} constant parameter β	[0, 1e-5, 5e-5, 1e-4, 5e-4]
LAM_{NE} constant parameter β	[0, 1e-5, 5e-5, 1e-4, 5e-4]
Temperature (K)	[273.15, 288.15, 298.15, 308.15, 318.15]
Charge and discharge C rates	[0.1, 0.5, 1, 1.5, 2]

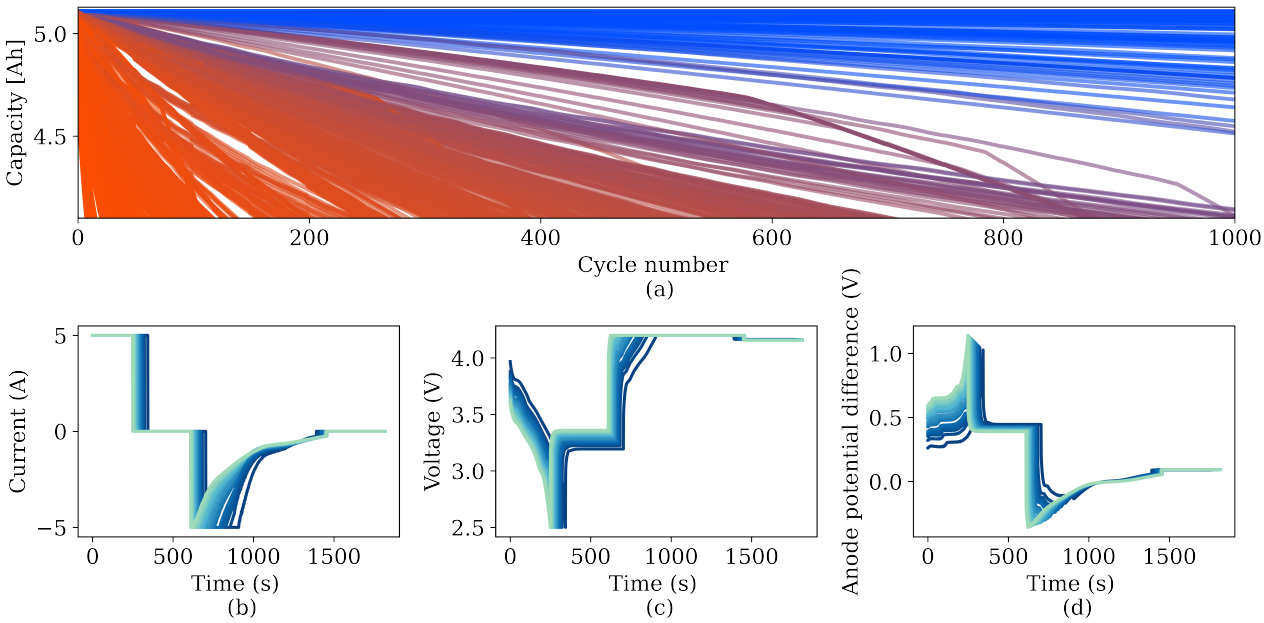

Figure S1: The overall simulation profiles generate synthetic data for plating potential estimation. (a) is the aging curves of all simulated cells; the cells with short lifetimes are shown in red, whereas the cells with long lifetimes are shown in blue. (b)-(d) shows a random cell current, voltage, and temperature profile used during cycling; the light blue represents the new cell state, and the darker blue represents the aged state.

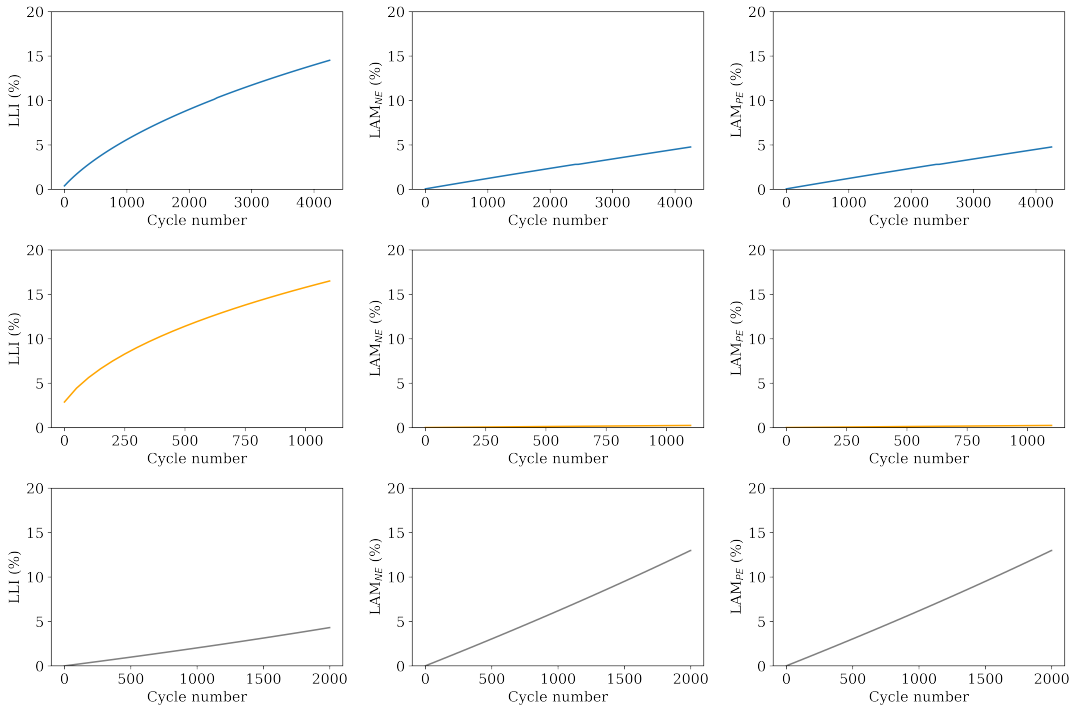

Figure S2: Nonlinear behavior of SoH indicators over the battery cycle life. Each color represents a different randomly selected cell.

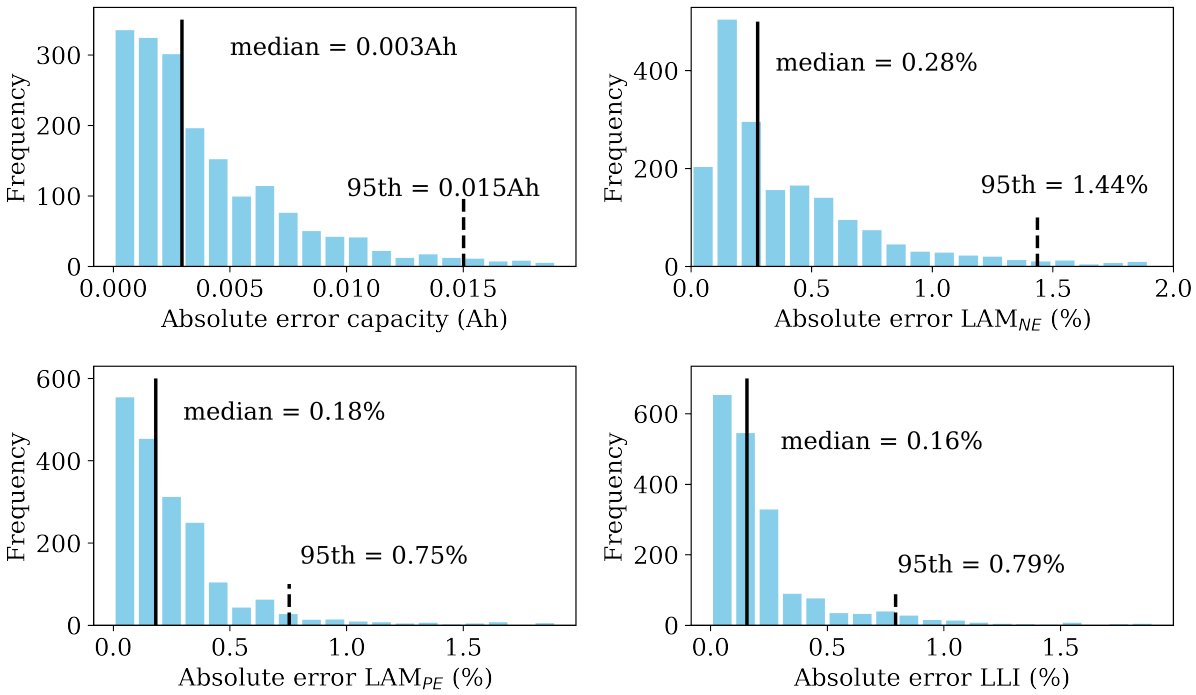

Figure S3: Estimation results of the four SoH indicators for batteries operated under 20%–50% SoC window.

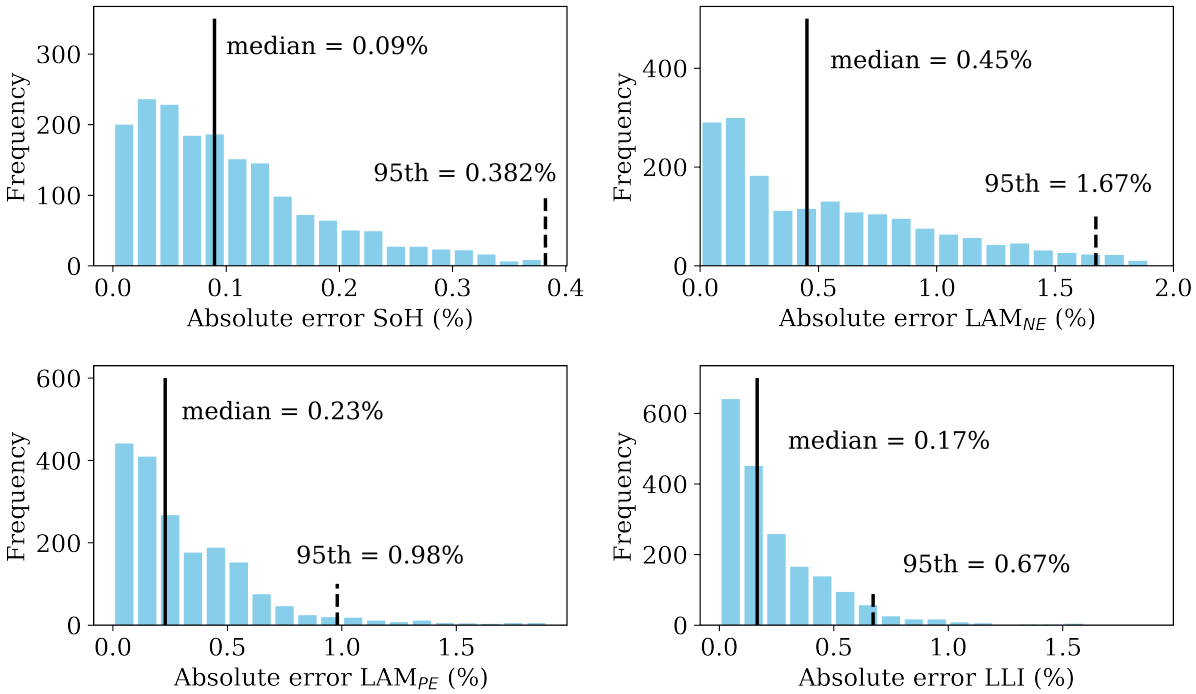

Figure S4: Estimation results of the four SoH indicators for batteries operated under 30%–60% SoC window.

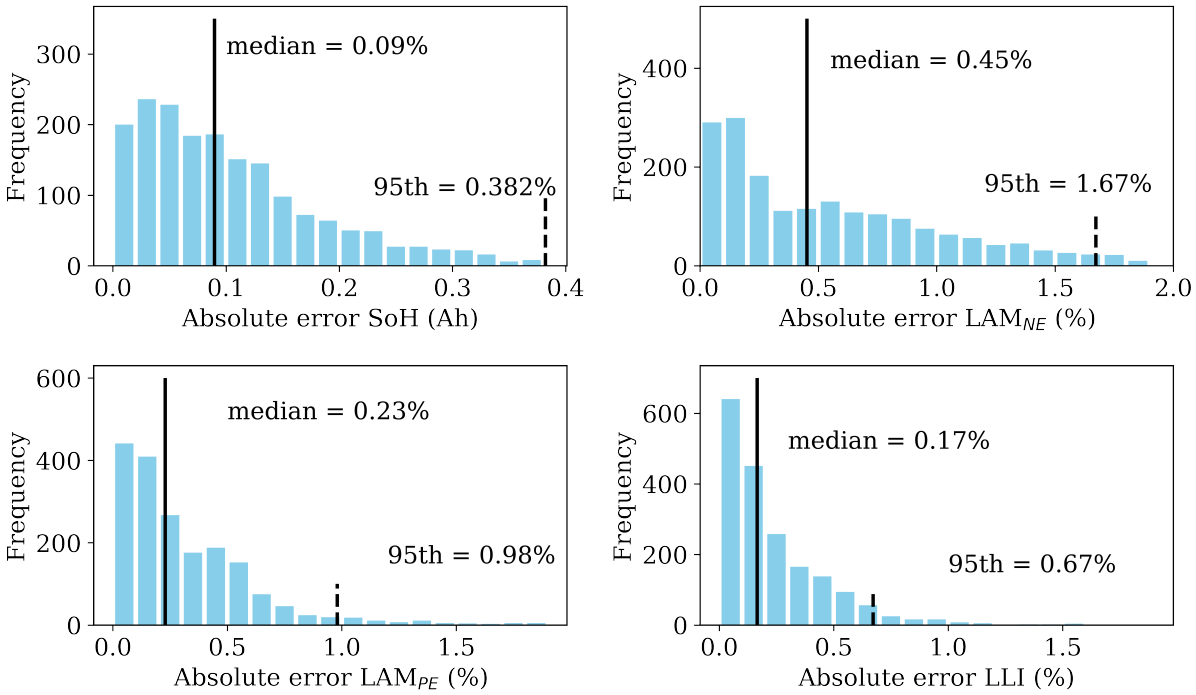

Figure S5: Estimation results of the four SoH indicators for batteries operated under 40%–70% SoC window.

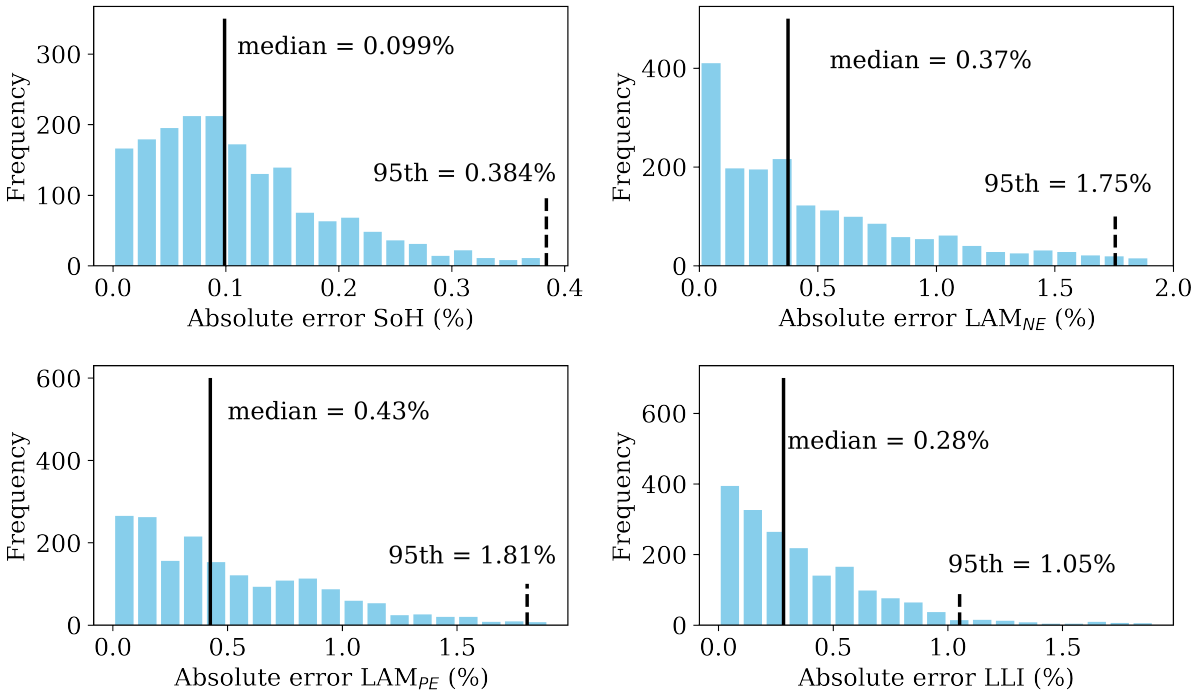

Figure S6: Estimation results of the four SoH indicators for batteries operated under 50%–80% SoC window.

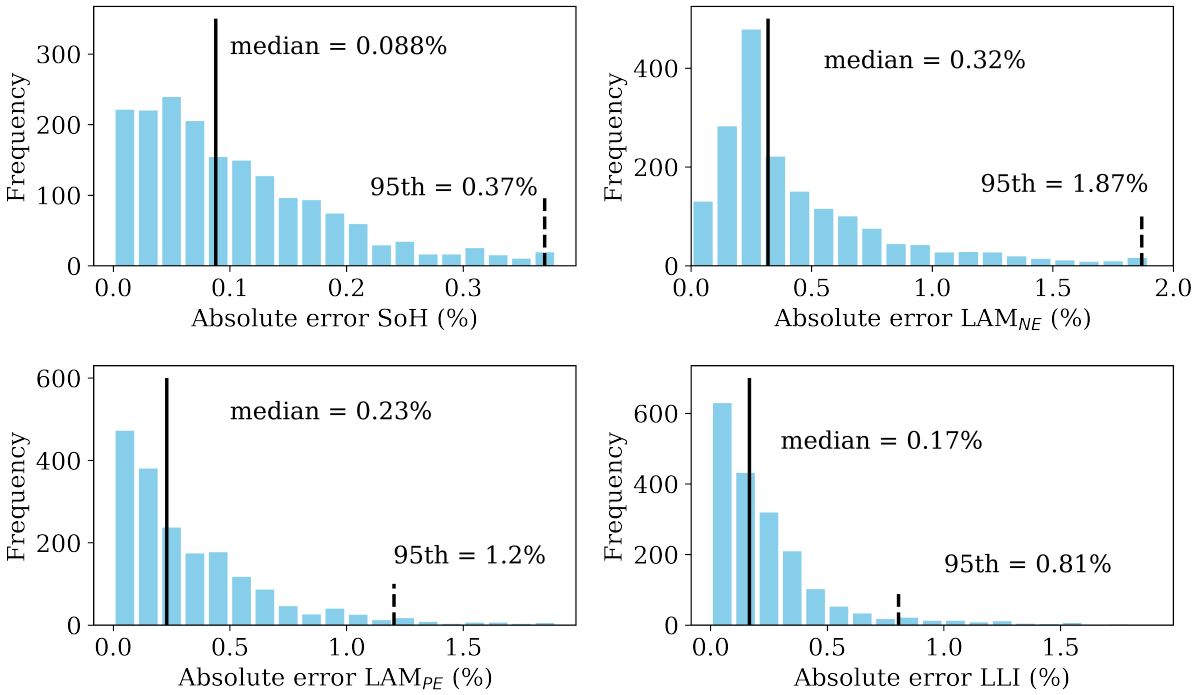

Figure S7: Estimation results of the four SoH indicators for batteries operated under 60%–90% SoC window.

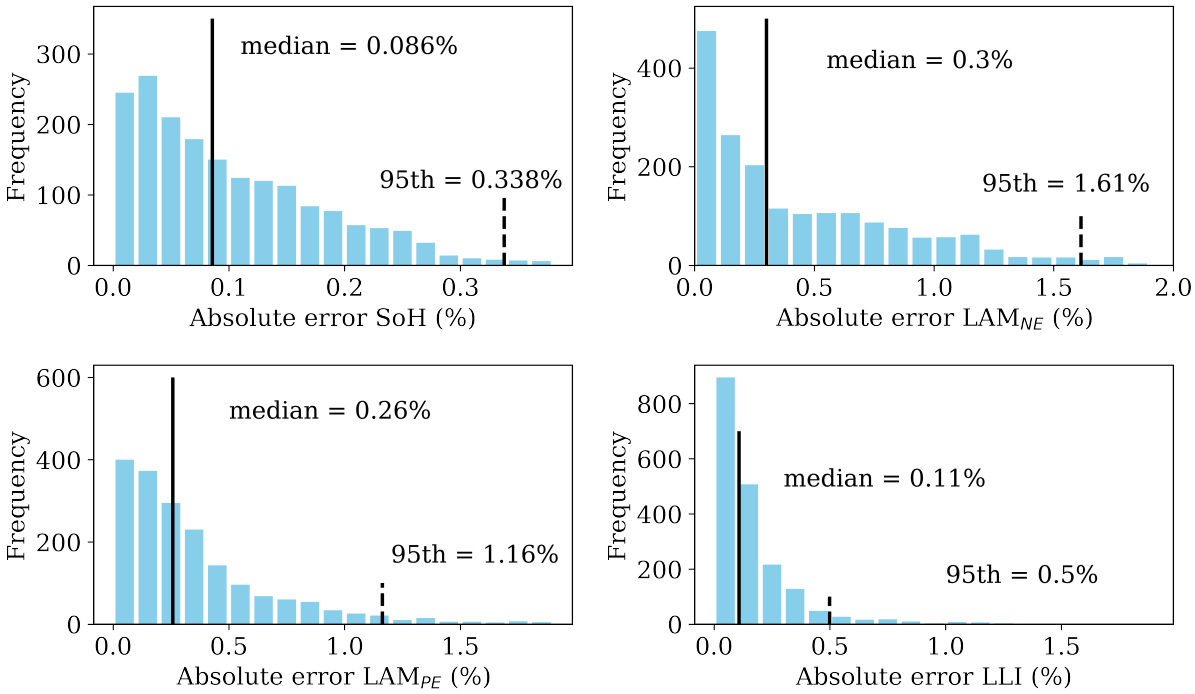

Figure S8: Estimation results of the four SoH indicators for batteries operated under 70%–100% SoC window.

7 Supplemental Note 7: Post-disassembly characterization studies of the CC-CV and CC-Cη cells

The stress difference between the two cycling strategies on the negative electrode was evident during the process of separating the separator from the negative electrode sheet. In the CC-CV cycling group, the separator and the graphite material were firmly attached, whereas in the CC-Cη group, the separation was relatively easy. We attribute this to a significant amount of lithium plating in the CC-CV group, where metallic lithium adhered firmly to the separator. The post-mortem images of the negative electrode material cycled with CC-CV and CC-Cη clearly exhibit different morphologies, as shown in Fig. S9. The rough surface and grey metallic color of the CC-CV cycled negative electrode strongly suggest the onset of lithium plating.

(a) CC-CV cycled cell

(b) CC-Cη cycled cell

Figure S9: Post-mortem images of the negative electrode material

8 Supplemental Note 8: Performance comparison of the cells with and without reference electrode.

The introduction of reference electrodes to measure the individual electrode potential is promising. However, the negative effect of the introduced reference electrode on the battery needs to be understood as well. Here, we conduct a series of performance comparison tests on the cells with or without reference electrodes to evaluate the difference between these two different cases.

Fig. S10 presents the C-rate performance tests of four cells: two equipped with reference electrodes and two without. As seen in the figure, the cells with reference electrodes exhibit marginally lower available capacity under different C-rates compared to those without reference electrodes. We attribute this slight reduction in capacity to the possibility that the reference electrode may block certain active material areas, resulting in a minor loss of available capacity.

Additionally, we performed AC impedance tests using Electrochemical Impedance Spectroscopy (EIS) with sinusoidal signals of 1 mA amplitude across frequencies ranging from 0.01 Hz to 10,000 Hz at four different states of charge. The comparison results are shown in Fig. S11. It is evident that the cell with a reference electrode exhibits slightly higher resistance than the cell without a reference electrode, the difference is minor and the impedance characteristics follow a similar behavior.

It is also important to note that the reference electrode we used is a ring reference electrode placed at the boundary of the separator, which differs from setups in some other studies that use only a metal line. This setup provides a

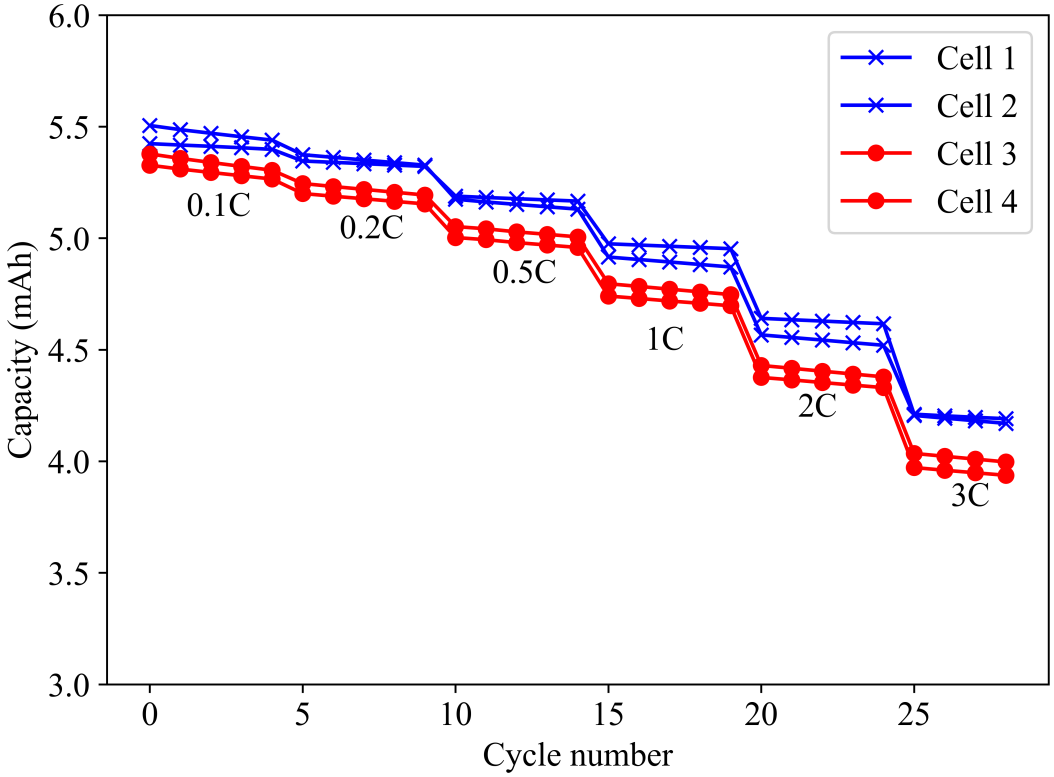

Figure S10: C-rate performance comparison of the cells equipped with and without reference electrode. Cells 3 and 4 are equipped with reference electrodes and Cells 1 and 2 are without reference electrodes.

more accurate and reliable measurement of the individual electrode potential. The layout of the three-electrode cell used in our experiments is provided in Fig. S12.

However, it is important to emphasize that this minor difference does not detract from our motivation to pursue the lithium plating potential-controlled charging strategy. The results indicate that the presence of a reference electrode does not significantly affect the key finding of our study: the ability to achieve faster charging without lithium plating, ultimately extending battery lifetime.

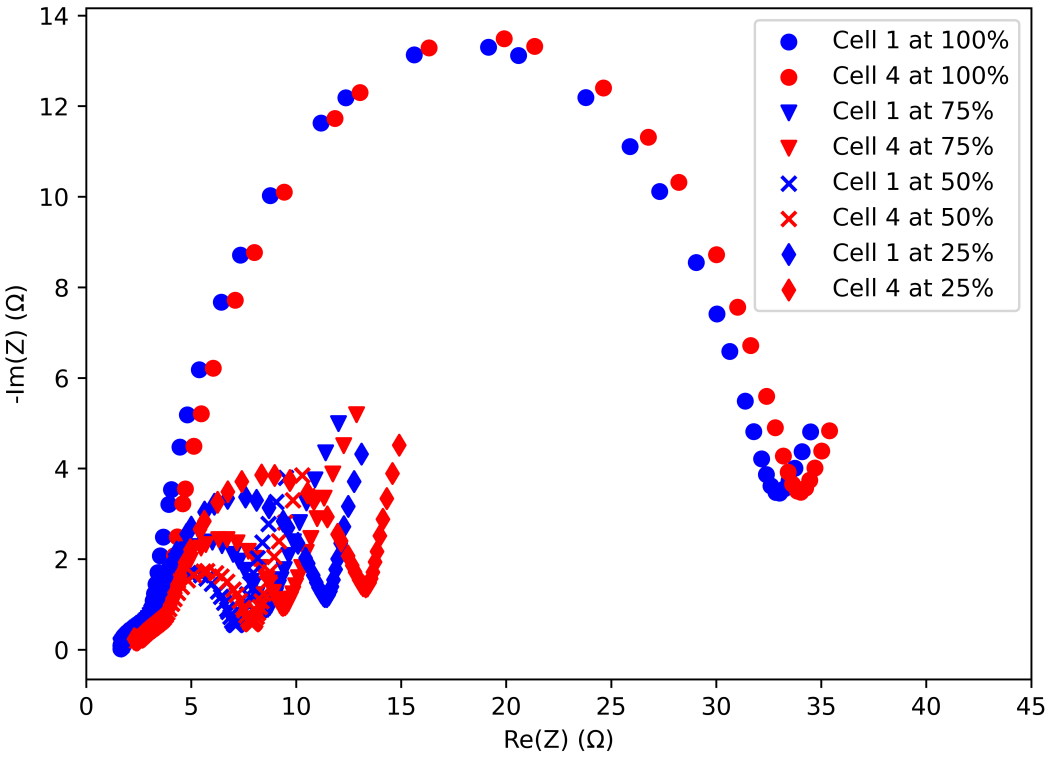

Figure S11: Comparison of the EIS curve for cells with and without reference electrode. Cell 4 is equipped with a reference electrode and Cell 1 is without a reference electrode.

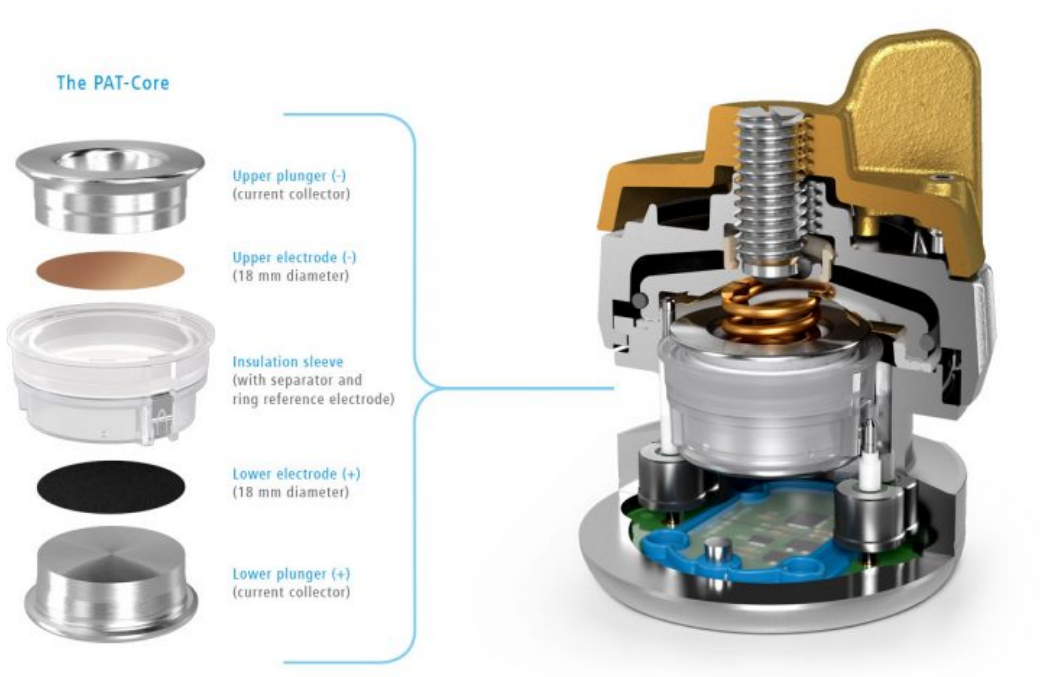

Figure S12: The layout of the used three-electrode cell setup [5].

References

[1] C. R. Birkl, M. R. Roberts, E. McTurk, P. G. Bruce, D. A. Howey, Degradation diagnostics for lithium ion cells, J. Power Sources 341 (2017) 373–386.

[2] D. Andre, C. Appel, T. Soczka-Guth, D. U. Sauer, Advanced mathematical methods of SOC and SOH estimation for lithium-ion batteries, J. Power Sources 224 (2013) 20–27.

[3] Y. Zhang, T. Wik, J. Bergström, C. Zou, State of health estimation for lithium-ion batteries under arbitrary usage using data-driven multi-model fusion, IEEE Trans. Transp. Electrif. (2023).

[4] C.-H. Chen, F. B. Planella, K. O'Regan, D. Gastol, W. D. Widanage, E. Kendrick, Development of experimental techniques for parameterization of multi-scale lithium-ion battery models, J. Electrochem. Soc. 167 (8) (2020).

[5] The pat-core: Enabling battery studies of unmatched quality, `https://https://www.el-cell.com/pat-series/the-pat-core-concept/`, accessed: 01-October-2024 (2024).